Micro- and nano-porosity of the active Alpine Fault zone, New Zealand

Martina Kirilova[1], Virginia Toy[1,2], Katrina Sauer[1], François Renard[3,4], Klaus Gessner[5], Richard Wirth[6], and Xianghui Xiao[7,8]

[1]Institut für Geowissenschafte, Johannes Gutenberg Universität-Mainz, J. J. Becher Weg 21D-55128, Mainz, Germany

[2]Department of Geology, University of Otago, PO Box 56, Dunedin 9054, New Zealand

[3]Department of Geosciences, The Njord Center, University of Oslo, Oslo 0316, Norway.

[4]Université Grenoble Alpes, Université Savoie Mont Blanc, CNRS, IRD, IFSTTAR, ISTerre, BP53, 38041 Grenoble, France.

[5]School of Earth Sciences, The University of Western Australia, 35 Stirling Highway, Crawley, WA 6009

[6]Helmholtz-Zentrum Potsdam, GFZ, Sektion 4.3, Telegrafenberg, 14473 Potsdam, Germany

[7]Advanced Photon Source, Argonne National Laboratory, Lemont, IL 60439, USA

[8]National Synchrotron Light Source II, Brookhaven National Laboratory, Upton, NY 11973, USA

Correspondence to: Martina Kirilova (martina.kirilova@uni-mainz.de)

Abstract

Porosity reduction in rocks from a fault core can cause elevated pore fluid pressures, and consequently influence the recurrence time of earthquakes. We investigated the porosity distribution in the New Zealand's Alpine Fault core in samples recovered during the first phase of the Deep Fault Drilling Project (DFDP-1B) by using two-dimensional nanoscale and three-dimensional microscale imaging. Synchrotron X-ray microtomography-derived analyses of open pore spaces show total microscale porosities in the range of 0.1 to 0.24%. These pores have mainly non-spherical, elongated, flat shapes and show subtle bipolar orientation. Transmission electron microscopy reveals that nanoscale pores ornament grain boundaries of the gouge material, especially clay minerals. Our data implies that: (i) the distribution of clay minerals controls the shape and orientation of the associated pores; (ii) porosity was reduced due to pressure solution processes; and (iii) mineral precipitation in fluid-filled pores can affect the mechanical behaviour of the Alpine Fault by decreasing the already critically low total porosity of the fault core, causing elevated pore fluid pressures, and/or introducing weak mineral phases, and thus lowering the overall fault frictional strength. We conclude that the current state of porosity in the Alpine Fault core is likely to play a key role in the initiation of the next fault rupture.

1. Introduction

Fault mechanics, fault structure and fluid flow properties of damaged fault rocks are intimately related (Gratier and Gueydan, 2007; Faulkner et al., 2010). Fault rupture is associated with intense brittle fracturing that enhances

porosity, and thus permeability, and therefore also possible rates and directions of fluid propagation within fault zones (Girault et al., 2018). Conversely, post seismic recovery mechanisms (gouge compaction and pressure solution processes) result in porosity, permeability and fluid flow propagation reductions (Renard et al, 2000; Faulkner et al., 2010; Sutherland et al., 2012). These processes may cause elevated pore fluid pressures within fault cores, and trigger frictional failure (Sibson, 1990; Gratier et al., 2003). Therefore, the state of porosity within rocks from fault cores can play a key role in fault slip.

The Alpine Fault of New Zealand is late in its seismic cycle (Cochran et al., 2017), so studying it allows us to investigate pre-earthquake conditions that may influence earthquake nucleation and rupture processes. Recently, drilling operations were undertaken in this fault zone to investigate the *in situ* conditions (Sutherland et al, 2012, 2017). Slug tests in the DFDP-1B borehole (Sutherland et al., 2012) and laboratory permeability measurements of core samples (Carpenter et al., 2014) indicate permeability decreases by six orders of magnitude with increasing proximity to the fault. Furthermore, Sutherland et al. (2012) documented a 0.53 MPa fluid pressure difference across the principal slip zone (PSZ) of the fault, which suggests that the fault core has significantly lower permeability than the surrounding cataclasite units. It is therefore interpreted to act as a fault seal that limits fluid circulation within its hanging wall (Sutherland et al., 2012). Permeability variations like this are closely associated with the porosity evolution of fault cores, and thus are likely to affect the fault strength and seismic properties (Sibson, 1990; Renard et al., 2000; Gratier and Gueydan, 2007).

In this study, we investigate the porosity distribution in rocks from the Alpine Fault core and consider the potential effects of this porosity on fault strength. We have measured open pore spaces in these rocks from X-ray computed tomography (XCT) datasets and examined pore morphology by implementing quantitative shape analyses and using transmission electron microscopy (TEM).

2. Geological setting

New Zealand`s Alpine Fault (Fig. 1a) is a major active crustal-scale structure that ruptures in a large earthquake every 291 ± 23 years, the last one of which occurred in 1717 (Cochran et al., 2017). The fault is the main constituent of the oblique transform boundary between the Australian Plate and the Pacific Plate, accommodating around 75% of the relative plate motion. Ongoing dextral strike-slip at 27 ± 5 mm yr^{-1} along the fault has resulted in a total strike-separation of ~ 480 km over the last 25 Ma (Norris and Cooper, 1995, 2001; Norris and Toy, 2014). In Neogene time, a dip-slip component added to the fault motion has resulted in more than 20 km of vertical uplift of the hanging wall (Norris and Cooper, 1995, 2001; Norris and Toy, 2014). Consequently, rocks comprising the hanging wall of the fault have been exposed in various outcrops, where they can be studied in detail. The amphibolite facies Alpine Schist is the metamorphic protolith of a ~ 1 km thick mylonite zone, which has been exhumed from depth and now structurally overlies an up to 50 m thick zone of brittlely deformed cataclasites and gouges (e.g. Norris and Cooper, 1995, 2001; Norris and Toy, 2014). These rocks have been investigated in outcrops and from samples collected in three boreholes during the two phases of the Deep Fault Drilling Project (DFDP-1A, DFDP-1B and DFDP-2B; Fig. 1a) along the Alpine Fault (Sutherland et al., 2012; Toy et al., 2015; Toy et al., 2017).

68 Most of the brittle shear displacement along the fault has been accommodated within the fault core, which includes
69 Principal Slip Zone (PSZ) gouges and cataclasite-series rocks (Toy et al., 2015). Both in surface outcrops and drill
70 core samples, the Alpine Fault manifests as a thin (5 to 20 cm thick) gouge zone with a predominantly random fabric
71 of clay-rich material (Toy et al., 2015; Schuck et al., 2020). This cohesive but uncemented layer has a significantly
72 finer grain size than the surrounding cataclasite units, which shows that the material was reworked only within this
73 layer, most probably as a result of ultracomminution due to multiple shear events under brittle conditions (Boulton
74 et al., 2012; Toy et al., 2015). The local presence of authigenic smectite clays (Schleicher et al., 2015) and calcite
75 and/or chlorite mineralization within sealed fractures and in the gouge matrix (Williams et al, 2017) indicate that
76 mineral reactions are restricted to an alteration zone within the fault core (Sutherland et al., 2012; Schuck et al.,
77 2020). The Alpine Fault core has been interpreted to have formed during a cyclical history of mineralization, shear,
78 and fragmentation (Toy et al., 2015). In addition, in the DFDP-1B borehole (Fig. 1b, Sutherland et al., 2012) fault
79 gouges occur at two distinct depths: 128.1 m (PSZ-1) and 143.85 m (PSZ-2), which shows that the slip was not
80 localized within a single gouge layer (Toy et al., 2015).

81 **3.   Sample description and analytical methods**

82 **3.1 Samples**

83 Porosity analyses were performed on four samples representing PSZ gouges and cataclasites of the Alpine Fault
84 core, which were recovered from the DFDP-1B borehole (Fig. 1b, c; Sutherland et al., 2012). These are DFDP-1B
85 58_1.9, DFDP-1B 69_2.48, DFDP-1B 69_2.54 and DFDP-1B 69_2.57. Sample nomenclature includes drill core run
86 number, section number, and centimeters measured from the top of each section. These samples were recovered
87 from drilled depth of 126.94 m, 143.82 m, 143.88 m and 143.91 m, respectively.

88 Detailed lithological and microstructural descriptions of the DFDP-1B drill core were carried out simultaneously
89 with, and after the drilling operations by the DFDP-1 Science Team, and these data were later summarized by Toy et
90 al. (2015). Samples DFDP-1B 58_1.9 and DFDP-1B 69_2.48 belong to the upper foliated cataclasite units (Fig. 1b,
91 c; Toy et al., 2015). These were described as ultracataclasites with gouge-filled shears located above PSZ-1 and
92 PSZ-2 respectively. Sample DFDP-1B 69_2.54 represents the gouge layer that defines PSZ-2, whereas sample
93 DFDP-1B 69_2.57 is composed of brown ultracataclasites that belong to the lower cataclasite unit (Fig. 1b, c; Toy et
94 al., 2015).

95 **3.2 X-ray computed tomography (XCT)**

96 We imaged the samples using absorption tomography, where the signal intensity depends on how electron density
97 and bulk density attenuate a monochromatic X-ray along its path through the material (e.g. Fusseis et al. 2014). We
98 acquired the X-ray microtomography data for this study at the 2-BM beamline of the Advanced Photon Source,
99 Argonne National Laboratories USA in December 2012. The non-cylindrical samples of ~7 mm height and ~ 4 mm
100 diameter were drilled parallel to the foliation and mounted on a rotary stage and imaged with a beam energy of 20
101 keV. A charge-couple device camera collected images at 0.25° rotation steps over 180° at sample detector distance

102 of 70 mm and FoV 2.81 mm. The voxel size was 1.3 µm. We have reconstructed the datasets with a filtered back-

103 projection parallel beam reconstruction into 32-bit gray level volumes consisting of 2083 * 2083 * 2083 voxels

104 using X-TRACT (Gureyev et al., 2011).

3.3 Analyses of XCT datasets

106 Data analyses and image processing were performed using the commercial software package Avizo 9.1 (Fig. 2).

107 Initially, the datasets were rescaled to 8-bit grey scale volumes for enhanced computer performance. In addition,

108 small volumes of interest were cropped from the whole volume before a non-local means filter was applied to

109 reduce noise (Buades et al., 2005). On the filtered gray-scale images, porosity was identified as the darkest phase

110 (Fig. 2a). The corresponding gray-scale values were thresholded, and the datasets were converted into binary form.

111 However, this threshold range also captured cracks within a sample, which are likely to result from depressurization

112 during core recovery (Fig. 2b). To omit the cracks, thresholded components with volumes larger than the volume of

113 200 face connected voxels (439.4 µm^3) were excluded from the binary label images by using the morphological

114 operation 'connected components' built in software Avizo 9.1. Clusters of connected components were then created

115 to visualize 3D volumes of segmented pore spaces (Fig. 2c).

116 Unfortunately, this methodology results in either loss of larger pores or inclusion of small cracks depending on the

117 implemented limit of connected components, and thus calculating total porosities includes significant bias.

118 Therefore, "connected components" limited up to 200 connected voxels were used only for visualization purposes.

119 Instead, the volumes and shape characteristics of segmented materials (including cracks) were exported from Avizo

120 software in numerical format, and volume distributions within a sample were plotted on a logarithmic scale in

121 Matlab (Fig. 3). Data up to a specific volume size were fit to a polynomial curve, and then the curve was

122 extrapolated to the X intercept, which is the expected maximum pore size (Fig. 3). Total porosities were then

123 estimated by integrating the curve, which excludes all volumes on the right side of the curve. Total porosities are

124 presented as a percentage of the whole sample volume (Fig. 3). The implemented equations are presented in

125 Supplementary material 1.

126 Pore shapes were analyzed on bivariate histograms plotted on Matlab by using the numerical pore characteristics,

127 previously extracted from Avizo software. Only pore volumes between 21.97 µm^3 (10 voxels) and 878.8 µm^3 (400

128 voxels) were included to avoid bias in the data due to insufficient voxel count and presence of cracks, respectively.

129 Individual pores in our dataset are separated (Fig. 2c), thus the covariance matrix of each pore was calculated, and

130 the three eigenvalues of this covariance matrix were extracted. These three values correspond to the three main

131 orthogonal directions in each pore (i.e. the longest, medium and shortest axes) and we use them as proxies to

132 describe pore geometry. Thus, their amplitudes provide information on the spatial extension of the pore and its

133 shape. The ratio between the medium and largest eigenvalues of each pore defines its elongation (Fig. 4), the ratio

134 between the smallest to the largest – its sphericity (Fig. 5), and the ratio of the smallest to the medium – its flatness

135 (Fig. 6).

136 The angles θ and φ that describe the orientation of the longest axis of each pore with respect to the main axis of the
137 3D scan were calculated. These angles were translated into trend and plunge and then plotted on a lower hemisphere
138 equal area stereographic projection with a probability density contour to display the distribution of pore unit
139 orientations (Fig. 7).

140 **3.4 Transmission electron microscopy (TEM)**

141 TEM images were collected on a FEI Tecnai G2 F20 X-Twin transmission electron microscope, located at the
142 German Research Centre for Geosciences (GFZ), Potsdam, Germany (Fig. 8). The instrument is equipped with field-
143 emission gun (FEG) electron source and high-angle annular dark-field (HAADF) Detector. Images were collected
144 from samples placed on a Gatan double-tilt holder at 200kV. TEM sample preparation was performed with focused
145 ion beam (FIB) milling at GFZ Potsdam using a HELIOS system operated at 30 kV.

146 **4. Results**

147 **4.1 XCT-derived characteristics of porosity**

148 All samples contain low total porosities, ranging from 0.1% to 0.24% (Fig. 3). However, it should be noted that the
149 lower cataclasite sample (DFDP-1B 69_2.57) has twice as much pore space (Fig. 3d) as any of the other samples.
150 The characterized pore size distributions range over almost three orders of magnitude for all samples (Fig. 3).
151 Furthermore, the expected maximum pore size volume was estimated to be largest in the PSZ-2 sample (DFDP-1B
152 69_2.54), reaching 862 μm^3 (Fig. 3c).

153 In all samples, shape analyses of pores with volumes between 21.97 μm^3 (10 voxels) and 878.8 μm^3 (400 voxels)
154 demonstrate predominantly elongated (Fig. 4), non-spherical (Fig. 5) and flat pore shapes (Fig. 6). This is
155 particularly pronounced for the smaller pore volumes. The number of elongated pores per sample is increasing in the
156 upper foliated cataclasites (Fig. 4a and b) with increasing proximity to PSZ-2, where most elongated pores occur
157 (Fig. 4c). Conversely, the lower cataclasite sample demonstrates proportionally fewer elongated pores within the
158 sample (Fig. 4d). The degree of sphericity is uniform for all samples, and pores appear as mainly non-spherical (Fig.
159 5). Few isolated spherical pores are manifested only by small pore volumes (Fig. 5). A trend of increasing the
160 number of flat pores is observed with increasing sample depth (Fig. 6), and most flat pores are detected in the lower
161 cataclasite (Fig. 6d).

162 The orientations of the individual pore units show two distinctive peaks with opposite vergence, defining bipolar
163 distributions of pore orientations (Fig. 7). The observed bipolarity is subtle in samples DFDP-1B 58_1.9 (Fig. 7a)
164 and DFDP-1B 69_2.48 (Fig. 7b), and more obvious in samples DFDP-1B 69_2.54 (Fig. 7c) and DFDP-1B 69_2.57
165 (Fig. 7d).

4.2 Microstructural characteristics of porosity

TEM characterization of the gouge material from PSZ-2 (sample DFDP-1B 69_2.54) reveals that the Alpine Fault gouges are composed of angular quartz and/or feldspar fragments (~200 nm in size), wrapped by smaller phyllosilicates (< 100 nm long). This random fabric is ornamented by nanoscale pores (< 50 nm), distributed along all grain and phase boundaries, especially abundant along clay minerals (Fig. 8a).

The gouge material also demonstrates phyllosilicate-rich areas, defined by an increase in the clay/clast ratio. In these zones, fine (< 100 nm long) and coarser (few µm long) clay grains coexist and are aligned in wavy fabric that surrounds sporadic protolith fragments (Fig. 8b). Pore spaces are again distributed along the boundaries of the constituent mineral grains but some of them are larger (~0.5 µm) with thin ellipsoidal or elongated shapes (Fig. 8b, c). These pores are commonly associated with inter-clay layer porosity. Large size pores are also observed along quartz-feldspar grains, where pores are associated with multiple grains and occasionally disrupt grain boundaries, thus were labelled as fracture porosity (Fig. 8d).

5.   Discussion

5.1 Characteristics of porosity within the Alpine Fault core

Porosity analyses of samples from, or in close proximity to the two PSZs encountered in the DFDP-1B drill core reveal total pore volumes between ~ 0.1 and 0.24% (Fig. 3). These values are significantly lower than the porosity estimates from other active faults in the world, such as: 0.2 to 5.7% total porosity in the core of the Nojima Fault, Japan (Surma et al., 2003) and 0 to 18% in the San Andreas Fault core (Blackburn et al., 2009). The Alpine Fault core contains total pore space volumes, comparable only with the lower porosities in these previous studies. It should be noted that the smallest pore spaces captured in the XCT datasets are 1.3 µm in size due to acquisition constrains, whereas nanoscale porosity was identified on the TEM images. Therefore, the estimated total porosities represent only minimum values of the open pore spaces in the Alpine Fault core.

TEM images presented here mainly focus on nano-scale materials (Fig. 8a, c, d) but were also used to describe the distribution of micro-porosity in these rocks (Figure 8b). The pores visible on grain and phase boundaries in figure 8b have similar sizes to the pores segmented on XCT images (> 1.3 µm in diameter), thus we conclude that this is the typical habit of both nano- and micro-pores within the Alpine Fault core (Fig. 8). In addition, both quantitative micro-porosity shape analyses (Fig. 4, 5 and 6) and nano-pores identified on TEM images (Fig. 8) reveal that a significant population of pores are predominantly non-spherical with elongated, flat shapes. We attribute this observation to the tendency of these pores to ornament clay minerals where pores are attained and elongated along their (001) planes (Fig. 8b, c and d).

Foliation in the upper cataclasites is defined by clay-sized phyllosilicates, that become more abundant with proximity to the PSZ (Toy et al., 2015), where weak clay fabric is developed (Schleicher et al., 2015). This gradual enrichment in clay minerals coincides with the subtle development of bipolar distributions of pore orientations with increasing sample depth (Fig. 7). This observation and the fact that pores are mainly attained along grain boundaries

200   of clays (Fig. 8) suggest that the distribution of clay minerals also controls pore orientations within the Alpine Fault

201   core. Previously, the phyllosilicate foliation in the Alpine Fault cataclasites has been used to define shear direction

202   (Toy et al., 2015). Thus, we speculate that pore orientations in these rocks are also systematically related to the

203   kinematic framework of the shear zone. If these pores represent remnants of fluid channels, their spatial orientation

204   is likely to reflect the fluid flow directions during deformation. To address this possibility more data for systematic

205   analyses of pore orientations are needed.

5.2 Porosity reduction within the Alpine Fault core

207   The comparatively lower porosity estimates of the Alpine Fault core than other active faults (e.g. the Nojima Fault,

208   Surma et al., 2003, and the San Andreas Fault, Blackburn et al., 2009) can be attributed to the fact that the Alpine

209   Fault is late in its seismic cycle and the last seismic event occurred in 1717 (Cochran et al., 2017). Porosity of the

210   fault core is considered to evolve during the seismic cycle when fault rupture can cause porosity increase up to 10%

211   (Marone et al., 1990), and the consequent healing mechanisms lead to porosity decrease over time due to mechanical

212   compaction of the fault gouge and/or elimination of pore spaces within the fault core due to pressure solution

213   processes (Sibson, 1990; Renard et al., 2000; Faulkner et al., 2010). TEM data presented here show abundance of

214   newly precipitated authigenic clays, wrapped around coarser clay minerals (Fig. 8b). Furthermore, delicate clay

215   minerals form fringe structures (Fig. 8a), and strain shadows (Fig. 8c) around larger quartz-feldspar grains. These

216   microstructural observations demonstrate that pressure solution processes operated within these rocks (Toy et al.,

217   2015).

218   Evidence for pressure solution processes has been previously documented in all units, comprising the Alpine Fault

219   core (Toy et al., 2015). Abundant precipitation of alteration minerals (Sutherland et al., 2012), calcite filled

220   intragranular and cross-cutting veins (Williams et al., 2017), and the occurrence of newly formed smectite clays

221   (Schleicher et al., 2015) indicate extensive fluid-rock reactions. In addition, anastomosing networks of opaque

222   minerals (such as graphite; Kirilova et al., 2017), which define foliation in the upper cataclasites (Toy et al., 2015),

223   have been interpreted to be concentrated by pressure solution processes during aseismic creep (Toy et al., 2015;

224   Gratier et al., 2011). The petrological characteristics of the Alpine Fault core lithologies identify solution transfer

225   mechanisms likely were the dominant mechanism for pore closure within these rocks.

226   Post-rupture porosity reduction is known to operate three to four times faster within fine-grained fault gouges than in

227   coarser-grained cataclasites (Walder and Nur, 1984; Sleep and Blanpied, 1992; Renard et al., 2000), which may

228   explain the differences in total porosity between the gouge-containing samples and the footwall ultracataclasite –

229   DFDP-1B 69-2.57 (Fig. 3). Furthermore, previous studies documented less carbonate and phyllosilicate filling of

230   cracks in the Alpine Fault footwall cataclasites as compared to the hanging wall cataclasites (Sutherland et al., 2012;

231   Toy et al., 2015), suggesting more reactive fluids are present and isolated withing the hanging wall of the Alpine

232   Fault. Thus, more intense dissolution-precipitation processes took place in the fault`s hanging wall, which very

233   likely resulted in more efficient porosity reduction, as demonstrated by our porosity estimates (Fig. 3).

234

5.3 Effects of porosity on the Alpine Fault strength

The extremely low porosity estimates presented here (Fig. 3) are consistent with the low permeabilities of 10^{-18} m^2 measured experimentally in clay-rich cataclasites and gouges from the Alpine Fault zone (Carpenter et al., 2014). In addition, the documented difference of total porosities between the hanging wall and footwall samples (Fig. 3) implies different intensity of pressure solution processes, and thus compartmented fluid propagation. Our data is comparable with the permeability measurements in that study (Carpenter et al., 2014) and yields increased confidence in their interpretation of a permeability gradient with distance from the PSZ, which itself acts as a hydraulic seal (Sutherland, et al., 2012). The existence of such a barrier to flow is characteristic for faults undergoing creep and locked faults (Rice, 1992; Labaume et al., 1997; Wiersberg and Erzinger, 2008). However, much higher permeabilities in the surrounding damaged rocks (Carpenter et al., 2014) allow fast propagation of fluids within them and can cause localization of high fluid pressures on one side or the other of a hydraulic seal (Sibson, 1990). Such fluid pressures can enhance gouge compaction and pressure solution processes within the fault core, which will eventually introduce zones of weakness and thus may trigger fault slip (Faulkner et al., 2010).

Previous studies and the observations presented here show that fluids were present in the Alpine Fault rocks. Fluid-filled pores represent a favorable environment for mineral precipitation, which can affect the fault strength in two ways: (i) Very small decrease of these critically low total porosities due to mineral precipitation would cause fluid pressurization, which is a well-known fault weakening mechanism described by Byerlee, 1990 and Sibson, 1990. However, this pressure increase will be slightly offset by inclusion of fluids into new hydrous minerals; (ii) deposition of frictionally weak phases (such as clay minerals and graphite), especially if they decorate grain contacts and/or form interlinked weak layers, would lower the overall frictional strength (Rutter et al., 1976; Niemeijer et al., 2010).

Precipitation of authigenic clay minerals was identified on our TEM data (Fig. 8) and also documented by previous studies (Schleicher et al., 2015). As well as having low frictional strengths (Moore and Lockner, 2004), clay minerals may also contribute to the formation of an impermeable seal if they form an aligned fabric, and thus can enhance the likelihood of fluid-pressurization in the fault rocks (Rice, 1992; Faulkner et al., 2010). In addition, graphite, which was previously documented in these rocks by previous studies (Kirilova et. al., 2017), may effectively weaken the fault due to mechanical smearing (Rutter et al., 2013) and/or localized precipitation within strained areas (Upton and Craw, 2008). Such graphite precipitation within shear surfaces was previously documented by Kirilova et al. (2017).

In summary, the presence of trapped fluids in the low porosity rocks of the Alpine Fault core possibly controls the mechanical behavior of the fault and could be responsible for future rupture initiation due to fluid pressurization and/or precipitation of weak mineral phases. This hypothesis is further supported by an experimental study showing that the DFDP-1 gouges are frictionally strong in the absence of elevated fluid pressure (Boulton et al., 2014).

6.   Conclusions

Analyses of XCT-datasets and TEM images of borehole samples from the core of the Alpine Fault reveal micro- and nanoscale pores, distributed along grain boundaries of the constituent mineral phases, especially clay minerals. The tendency of these pores to ornament clays defines their predominantly non-spherical, elongated, flat shapes and the bipolar distribution of pore orientations. The documented extremely low total porosities (from 0.1 to 0.24 %) in these rocks suggest effective porosity reduction. Microstructural observations presented here and documented in previous studies indicate that pressure solution processes were the dominant healing mechanism, and that fluids were present in these rocks. Therefore, fluid-filled pores may be places where elevated pore fluid pressures develop, due to further mineral precipitation that decreases the already critically low total porosities. Alternatively, they may also facilitate deposition of weak mineral phases (such as clay minerals and graphite) that may very effectively weaken the fault. We conclude that the current state of the fault core porosity is possibly a controlling factor on the mechanical behaviour of the Alpine Fault and will likely play a key role in the initiation of the next fault rupture.

Data availability.

Matlab code and numerical data of pore volumes can be found in Supplementary material 1.

Authors contribution

Kirilova reconstructed, processed, and analysed the XCT datasets presented here, interpreted the TEM data and prepared the manuscript. Most of this work was performed during Kirilova's PhD under the academic guidance of Toy. Toy and Gessner collected the XCT data with technical support by Xiao. Renard and Sauer contributed with valuable discussion about XCT data analyses. Wirth enabled TEM data acquisition and provided his expertise on TEM data interpretation. The final version of this manuscript benefits from collective intellectual input.

Competing interests

The authors declare that they have no conflict of interest.

Acknowledgments

We gratefully acknowledge funding from the Advances Photon Source (GUP 31177). This research used resources of the Advanced Photon Source, a U.S. Department of Energy (DOE) Office of Science User Facility operated for the DOE Office of Science by Argonne National Laboratory under Contract No. DE-AC02-06CH11357. Avizo workstation was built at the University of Otago with financial support provided by Nvidia, Corporation Royal Society of New Zealand`s Rutherford fellowships (16-UOO-001), the Ministry of Business and Innovation`s Endeavor Fund (C05X1605/GNS-MBIE00056), and a subcontract to the Tectonics and Structure of Zealandia Program at GNS Science (GNS-DCF00020). Publishing bursary funding provided by the University of Otago is greatly appreciated. We thank Sherry Mayo for helping with the reconstruction process of XCT data and Andrew Squelch for providing use of the Avizo workstation, located at CSIRO, Perth, Australia during the initial data

300 analyses. Special thanks to Reed Debaets for assistance with the development of Matlab code. Klaus Gessner

301 publishes with permission of the Executive Director, Geological Survey of Western Australia.

References

303 Berryman, K. R., Cochran, U. A., Clark, K. J., Biasi, G. P., Langridge, R. M., and Villamor, P., 2012, Major

304 earthquakes occur regularly on an isolated plate boundary fault, Science, 336(6089), 1690-1693.

305 Blackburn, E. D., Hadizadeh, J., and Babaie, H. A., 2009, A microstructural study of SAFOD gouge from actively

306 creeping San Andreas Fault zone: Implications for shear localization models, *in* AGU Fall Meeting Abstracts.

307 Buades, A., Coll, B. and Morel, J. M., 2005, A non-local algorithm for image denoising, *in* Computer Vision and

308 Pattern Recognition, IEEE Computer Society Conference, Vol. 2, pp. 60-65.

309 Boulton, C., Carpenter, B. M., Toy, V., and Marone, C., 2012, Physical properties of surface outcrop cataclastic

310 fault rocks, Alpine Fault, New Zealand, Geochemistry, Geophysics, Geosystems, 13, Q01018,

311 doi:10.1029/2011GC003872.

312 Boulton, C., Moore, D. E., Lockner, D. A., Toy, V. G., Townend, J., and Sutherland, R., 2014, Frictional properties

313 of exhumed fault gouges in DFDP-1 cores, Alpine Fault, New Zealand, Geophysical Research Letters, 41(2), 356-

314 362.

315 Byerlee, J., 1990, Friction, overpressure and fault normal compression, Geophysical Research Letters, 17(12), 2109-

316 2112.

317 Carpenter, B. M., Kitajima, H., Sutherland, R., Townend, J., Toy, V. G., and Saffer, D. M., 2014, Hydraulic and

318 acoustic properties of the active Alpine Fault, New Zealand: Laboratory measurements on DFDP-1 drill core, Earth

319 and Planetary Science Letters, 390, 45-51.

320 Cochran, U. A., Clark, K. J., Howarth, J. D., Biasi, G. P., Langridge, R. M., Villamor, P., ... and Vandergoes, M. J.,

321 2017, A plate boundary earthquake record from a wetland adjacent to the Alpine fault in New Zealand refines

322 hazard estimates, Earth and Planetary Science Letters, 464, 175-188.

323 Faulkner, D. R., Jackson, C. A. L., Lunn, R. J., Schlische, R. W., Shipton, Z. K., Wibberley, C. A. J., and Withjack,

324 M. O., 2010, A review of recent developments concerning the structure, mechanics and fluid flow properties of fault

325 zones, Journal of Structural Geology, 32(11), 1557-1575.

326 Fusseis, F., Xiao, X., Schrank, C., and De Carlo, F., 2014, A brief guide to synchrotron radiation-based

327 microtomography in (structural) geology and rock mechanics, Journal of Structural Geology, 65, 1-16.

328 Girault, F., Adhikari, L. B., France-Lanord, C., Agrinier, P., Koirala, B. P., Bhattarai, M., and Perrier, F., 2018,
329 Persistent CO 2 emissions and hydrothermal unrest following the 2015 earthquake in Nepal, Nature
330 Communications, 9(1), 2956.

331 Gratier, J.-P., Favreau, P., and Renard, F., 2003, Modelling fluid transfer along California faults when integrating
332 pressure solution crack sealing and compaction processes, Journal of Geophysical Research, 108, 2104,
333 doi:10.1029/2001JB000380, B2.

334 Gratier, J. P., 2011, Fault permeability and strength evolution related to fracturing and healing episodic processes
335 (years to millennia): the role of pressure solution, Oil and Gas Science and Technology–Revue d'IFP Energies
336 nouvelles, 66(3), 491-506.

337 Gratier, J. P., and Gueydan, F., 2007, Effect of Fracturing and Fluid–Rock Interaction on Seismic Cycles, Tectonic
338 Faults: Agents of Change on a Dynamic Earth, 95, 319e356.

339 Gureyev, TE, Nesterets, Y, Ternovski, D, Wilkins, SW, Stevenson, AW, Sakellariou, A and Taylor, JA 2011,
340 Toolbox for advanced x-ray image processing, in Advances in Computational Methods for X-Ray Optics II edited
341 by M Sanchez del Rio and O Chubar, Advances in Computational Methods for X-Ray Optics II, San Diego, USA,
342 21-25 August 2011: SPIE - The International Society of Optics and Photonics 8141.

343 Janssen, C., Wirth, R., Reinicke, A., Rybacki, E., Naumann, R., Wenk, H. R., and Dresen, G., 2011, Nanoscale
344 porosity in SAFOD core samples (San Andreas Fault), Earth and Planetary Science Letters, 301(1), 179-189.

345 Labaume, P., Maltman, A. J., Bolton, A., Tessier, D., Ogawa, Y., and Takizawa, S. 1997, Scaly fabrics in sheared
346 clays from the décollement zone of the Barbados accretionary prism, *in* Shipley, T.H., Ogawa, Y., Blum, P., and
347 Bahr, J.M. (Eds.), Proceedings of the Ocean Drilling Program Scientific Results, 59-78.

348 Kirilova, M., Toy, V. G., Timms, N., Halfpenny, A., Menzies, C., Craw, D., ... and Carpenter, B. M., 2017, Textural
349 changes of graphitic carbon by tectonic and hydrothermal processes in an active plate boundary fault zone, Alpine
350 Fault, New Zealand, Geological Society, London, Special Publications, 453, SP453-13.

351 Marone, C., Raleigh, C. B., and Scholz, C. H., 1990, Frictional behavior and constitutive modeling of simulated
352 fault gouge, Journal of Geophysical Research: Solid Earth, 95(B5), 7007-7025.

353 Niemeijer, A., Marone, C., and Elsworth, D., 2010, Fabric induced weakness of tectonic faults, Geophysical
354 Research Letters, 37, L03304, doi:10.1029/2009GL041689.

355 Norris, R. J., and Cooper, A. F., 1995, Origin of small-scale segmentation and transpressional thrusting along the
356 Alpine fault, New Zealand. Geological Society of America Bulletin, 107(2), 231-240.

357   Norris, R. J., and Cooper, A. F., 2001, Late Quaternary slip rates and slip partitioning on the Alpine Fault, New
358   Zealand. Journal of Structural Geology, 23(2), 507-520.

359   Norris, R. J., and Toy, V. G., 2014, Continental transforms: A view from the Alpine Fault, Journal of Structural
360   Geology, 64, 3-31.

361   Renard, F., Gratier, J. P., and Jamtveit, B., 2000, Kinetics of crack-sealing, intergranular pressure solution, and
362   compaction around active faults, Journal of Structural Geology, 22(10), 1395-1407.

363   Rice, J. R., 1992, Fault stress states, pore pressure distributions, and the weakness of the San Andreas fault,
364   International Geophysics, 51, 475-503.

365   Rutter, E. H., and Elliott, D., 1976, The kinetics of rock deformation by pressure solution, Philosophical
366   Transactions for the Royal Society of London, Series A, Mathematical and Physical Sciences, 283, 203-219.

367   Rutter, E. H., Hackston, A. J., Yeatman, E., Brodie, K. H., Mecklenburgh, J., and May, S. E., 2013, Reduction of
368   friction on geological faults by weak-phase smearing, Journal of Structural Geology, 51, 52-60.

369   Schleicher, A. M., Sutherland, R., Townend, J., Toy, V. G., and Van Der Pluijm, B. A., 2015, Clay mineral
370   formation and fabric development in the DFDP-1B borehole, central Alpine Fault, New Zealand, New Zealand
371   Journal of Geology and Geophysics, 58(1), 13-21.

372   Schuck, B., Schleicher, A. M., Janssen, C., Toy, V. G., and Dresen, G., 2020, Fault zone architecture of a large
373   plate-bounding strike-slip fault: a case study from the Alpine Fault, New Zealand. Solid Earth, 11(1), 95-124.

374   Secor, D. T.,1965, Role of fluid pressure in jointing, American Journal of Science, 263(8), 633-646.

375   Sibson, R. H., 1990, Conditions for fault-valve behaviour, Geological Society, London, Special Publications, 54(1),
376   15-28.

377   Sleep, N. H., and Blanpied, M. L., 1992, Creep, compaction and the weak rheology of major faults, Nature,
378   359(6397), 687-692.

379   Surma, F., Géraud, Y., and Pezard, P., 2003, Porosity network of the Nojima fault zone in the Hirabayashi hole
380   (Japan), *in* EGS-AGU-EUG Joint Assembly.

381   Sutherland, R., Eberhart-Phillips, D., Harris, R. A., Stern, T., Beavan, J., Ellis, S Henrys, S., Cox, S., Norris, R.J.,
382   Berryman, K.R. and Townend, J., 2007, Do great earthquakes occur on the Alpine fault in central South Island, New
383   Zealand?, In: A continental plate boundary: tectonics at South Island, New Zealand, Geophysical Monograph,
384   American Geophysical Union, 235-251.

385   Sutherland, R., Toy, V. G., Townend, J., Cox, S. C., Eccles, J. D., Faulkner, D. R Prior, D.J., Norris, R.J., Mariani,

386   E., Boulton, C. and Carpenter, B.M., 2012, Drilling reveals fluid control on architecture and rupture of the Alpine

387   fault, New Zealand, Geology, 40(12), 1143-1146.

388   Sutherland, R., Townend, J., Toy, V., Upton, P., Coussens, J., Allen, M., and Boles, A., 2017, Extreme

389   hydrothermal conditions at an active plate-bounding fault, Nature, 546, 137-140, doi: 10.1038/nature22355.

390   Toy, V. G., Boulton, C. J., Sutherland, R., Townend, J., Norris, R. J., Little, T. A., and Scott, H., 2015, Fault rock

391   lithologies and architecture of the central Alpine fault, New Zealand, revealed by DFDP-1 drilling, Lithosphere,

392   L395-1.

393   Toy, V. G., Sutherland, R., Townend, J., Allen, M., Becroft, L., Boles, A., Boulton., C., Carpenter, B., Cooper, A.,

394   Cox, S., Daube, C., Faulkner., D., Halfpenny, A., Kato, N., Keys, S., Kirilova, M., Kometani, Y., Little, T., Mariani,

395   E., Melosh, B., Menzies, C., Morales, L., Morgan, C., Mori, C., Niemeijer, A., … and Zimmer, M., 2017, Bedrock

396   Geology of DFDP-2B, Central Alpine Fault, New Zealand, New Zealand Journal of Geology and Geophysics.,

397   60(4), 497-518.

398   Upton P. and Craw D., 2008, Modelling the role of graphite in development of a mineralised mid-crustal shear zone,

399   Macraes mine, New Zealand, Earth and Planetary Science Letters 266: 245-255.

400   Walder, J., and Nur, A., 1984, Porosity reduction and crustal pore pressure development, Journal of Geophysical

401   Research: Solid Earth, 89(B13), 11539-11548.

402   Walsh, J. B., 1965, The effect of cracks on the uniaxial elastic compression of rocks, Journal of Geophysical

403   Research, 70(2), 399-411.

404   Wiersberg, T and Erzinger, J 2008, Origin and spatial distribution of gas at seismogenic depths of the San Andreas

405   Fault from drill-mud gas analysis: Applied Geochemistry, v. 23, no. 6, p. 1675-1690.

406   Williams, J. N., Toy, V. G., Smith, S. A and Boulton, C., 2017, Fracturing, fluid-rock interaction and mineralisation

407   during the seismic cycle along the Alpine Fault, Journal of Structural Geology, 103, 151-166.

409
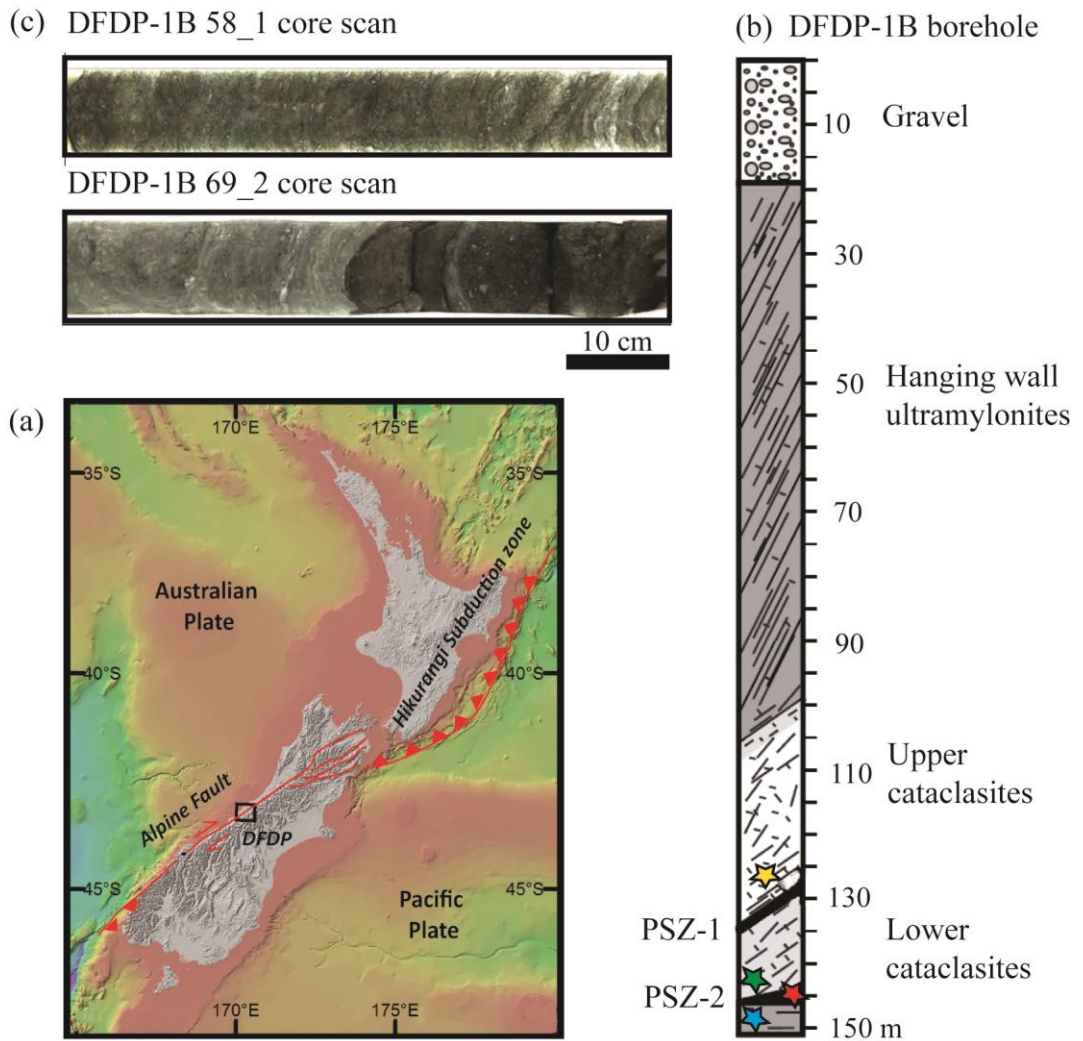
Figure 1. (a) Location map of DFDP drill sites (a bathymetric map compiled by NIWA). Drill site coordinates: 43°17′5″S, 170°24′22″E (b) Schematic diagram of the sampled lithologies in DFDP-1B borehole (modified after Sutherland et al., 2012). (c) Scans of DFDP-1B drill core. Samples were collected from the locations indicated with stars: yellow – DFDP-1B 58_1.9; green – DFDP-1B 69_2.48; red – DFDP-1B 69_2.54; blue – DFDP-1B 69_2.57.

DFDP - 1B 69-2.57
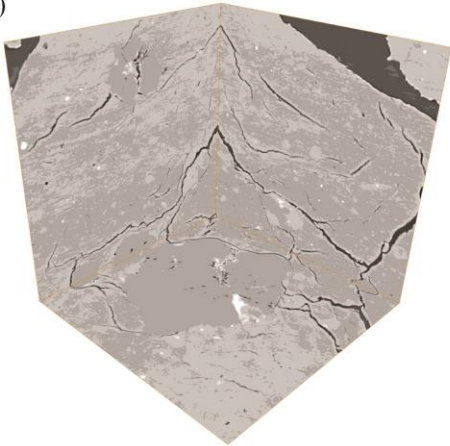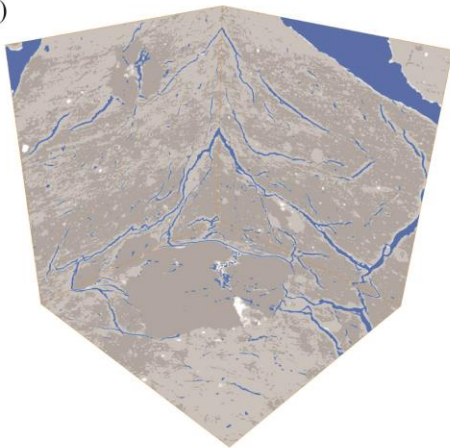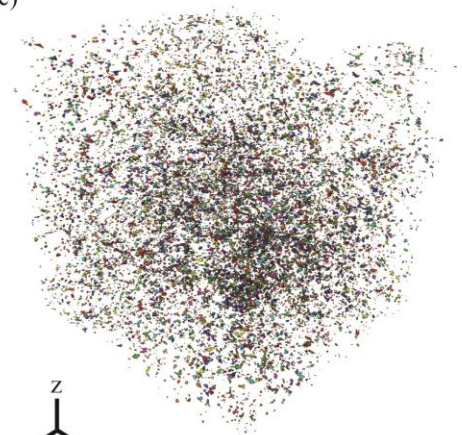
414
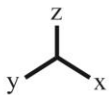
415 **Figure 2.** X-ray tomography data processing workflow. (a) Gray scale images in xy, xz and yz directions (b)
416 Threshold of the darkest gray scale phase in each sample, corresponding to voids (pores and fractures); (c) 3D
417 volume of the segmented pore spaces after removal of the fractures due to sample decompaction and coring
418 damaging effects were removed.
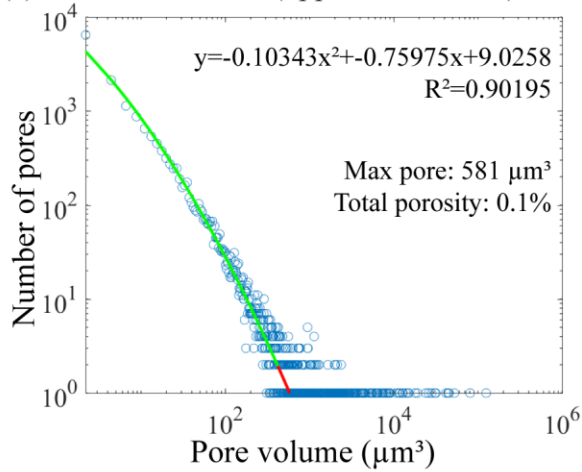
419
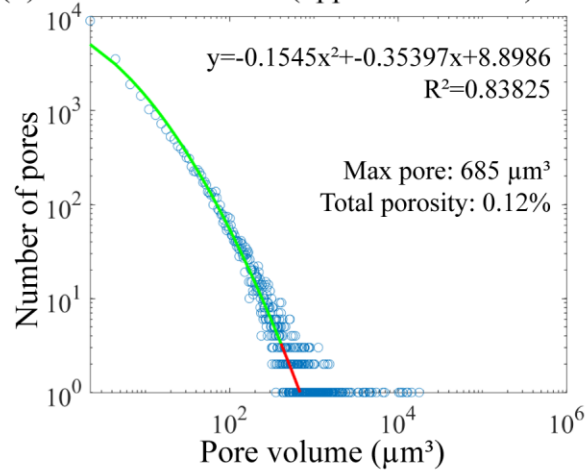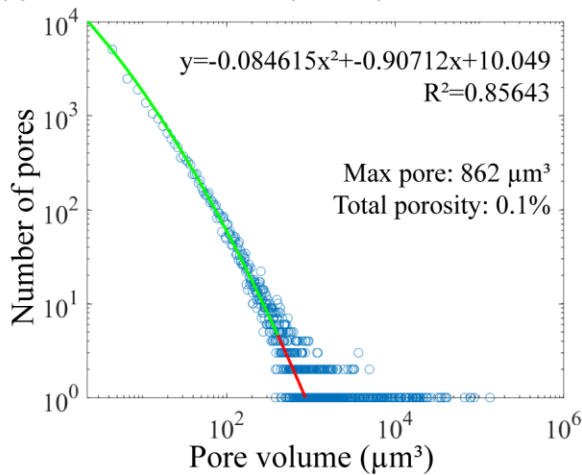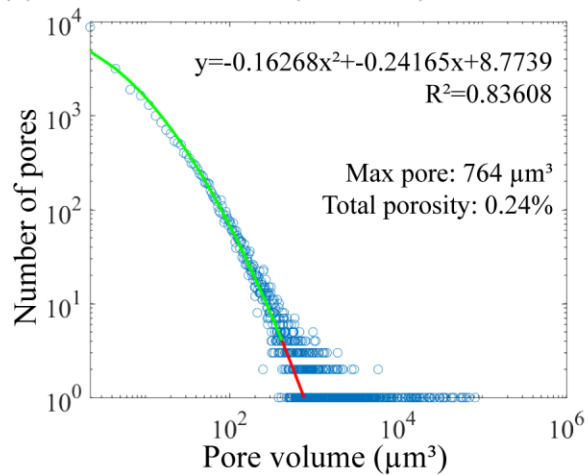
Figure 3. Plots of pore volume versus number of pores for each sample. Estimates of total porosity and size of the maximum expected pore are also shown, as well as the curve fitting function for each dataset.
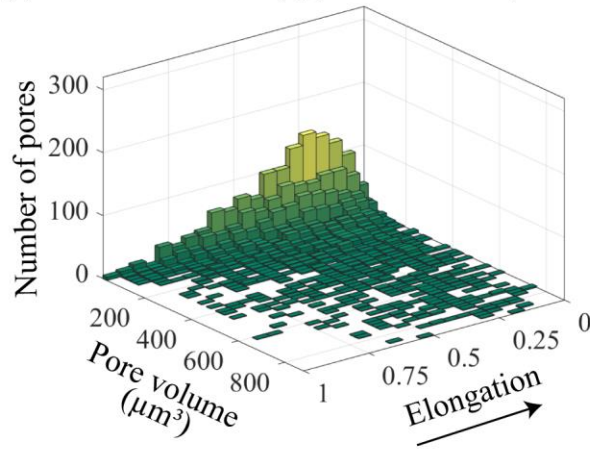
420

421

422
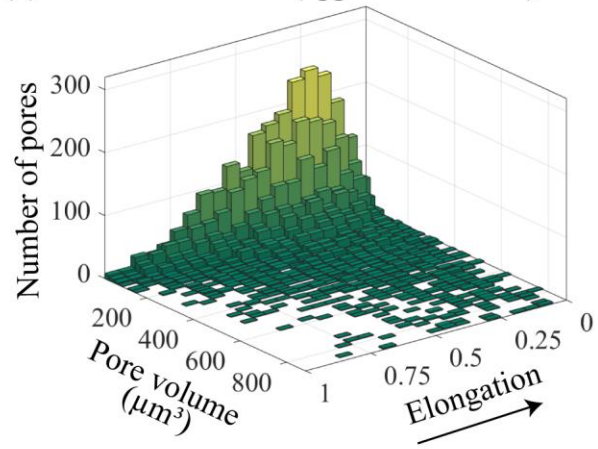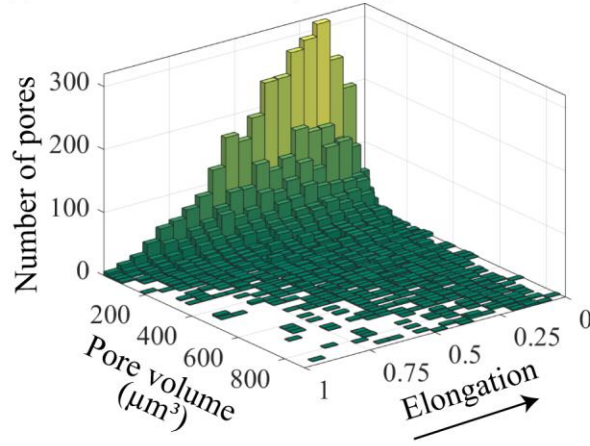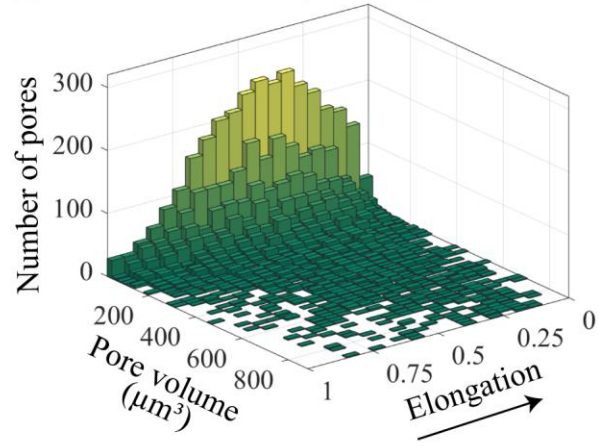
Figure 4. Bivariate histograms showing elongation versus pore volume (μm^3) and number of pores for each sample.

The arrow indicates the direction of increasing elongation.
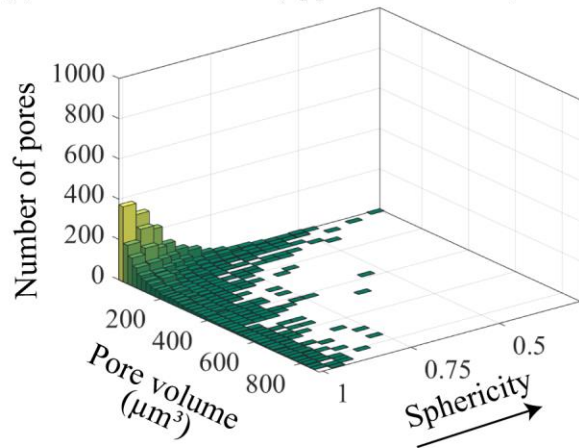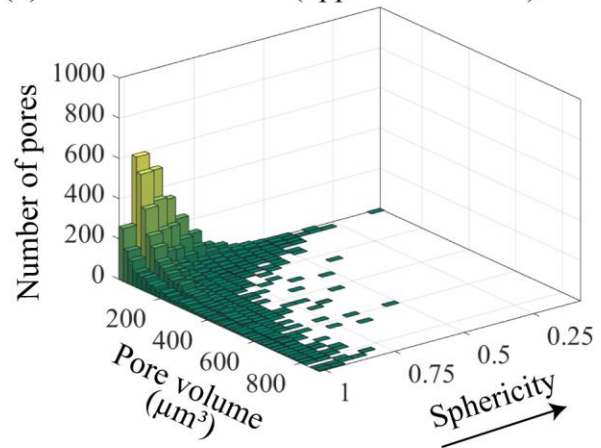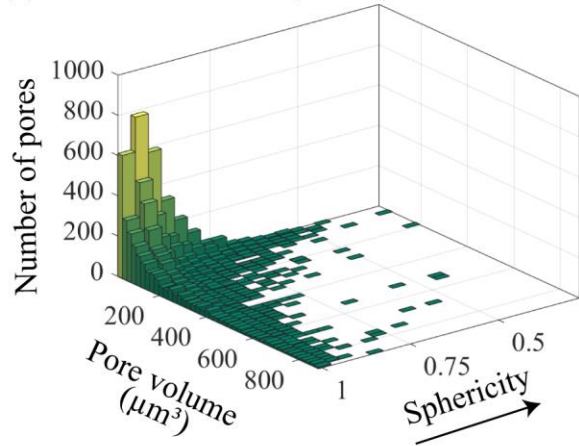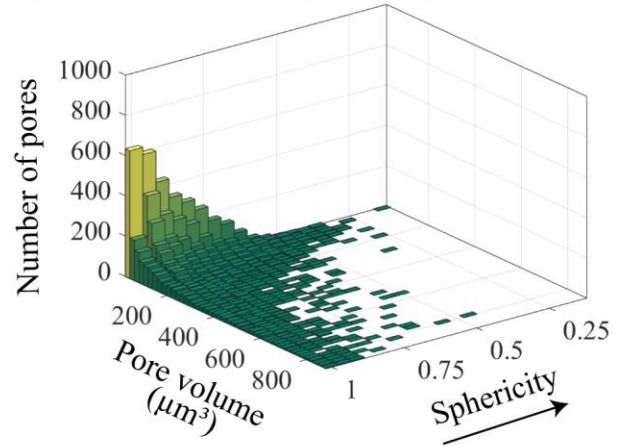
425

426 **Figure 5.** Bivariate histograms showing sphericity versus pore volume (μm^3) and number of pores for each sample.

427 The arrow indicates the direction of increasing sphericity.
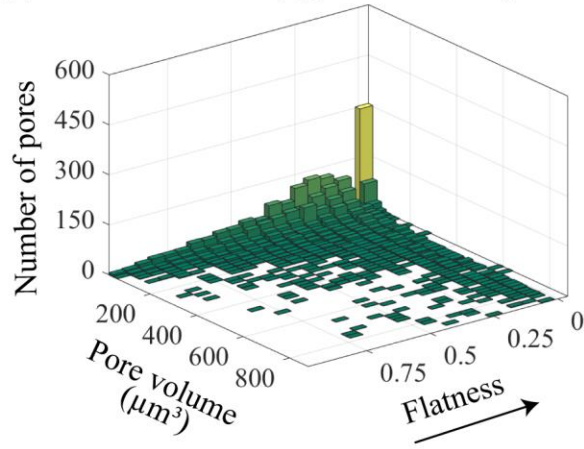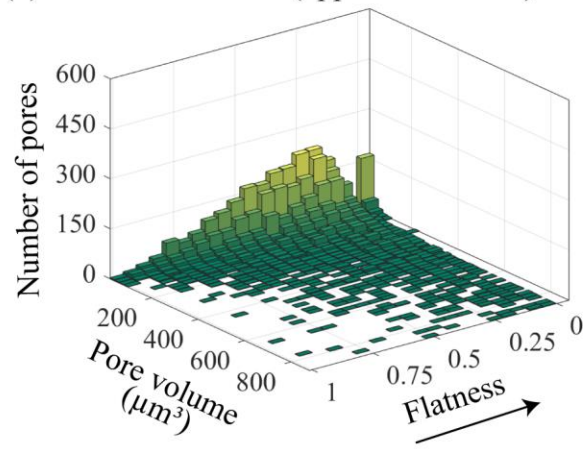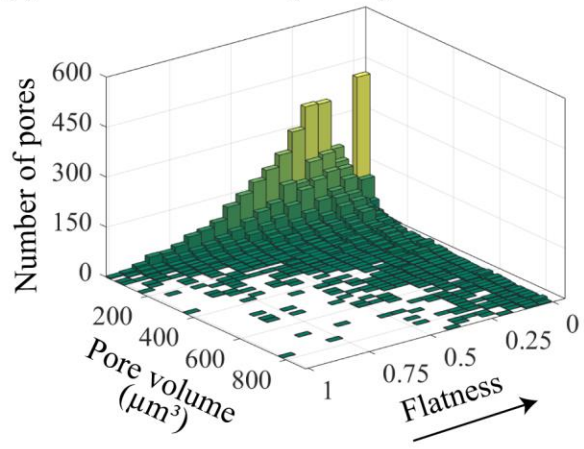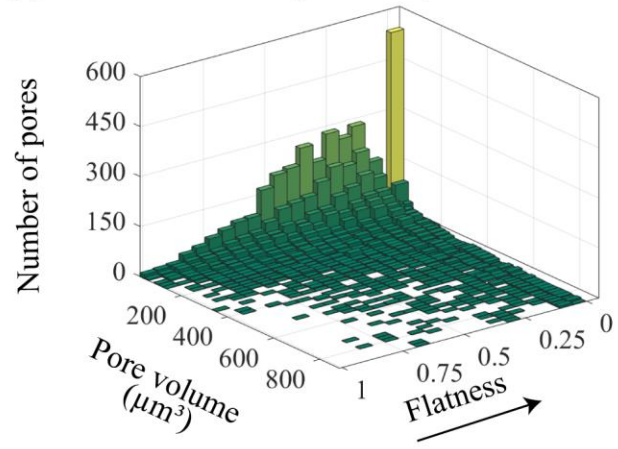
428

429 **Figure 6.** Bivariate histograms showing flatness versus pore volume (μm³) and number of pores for each sample.

430 The arrow indicates the direction of increasing flatness.
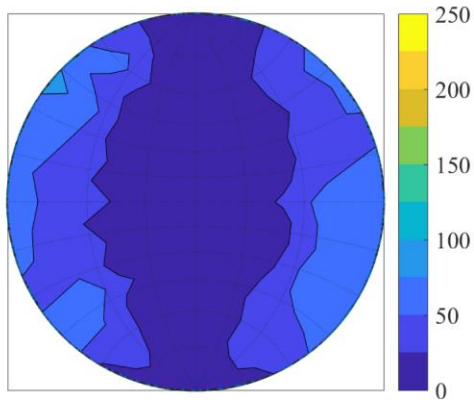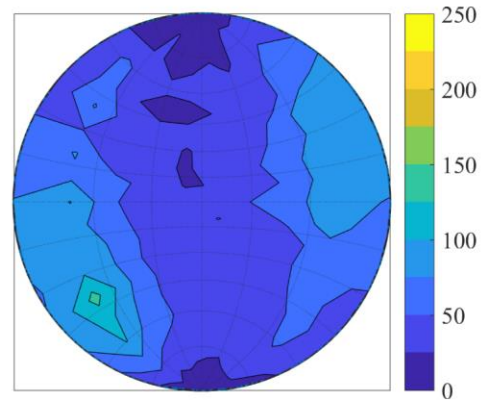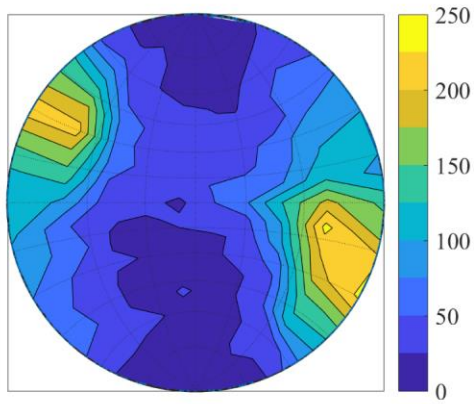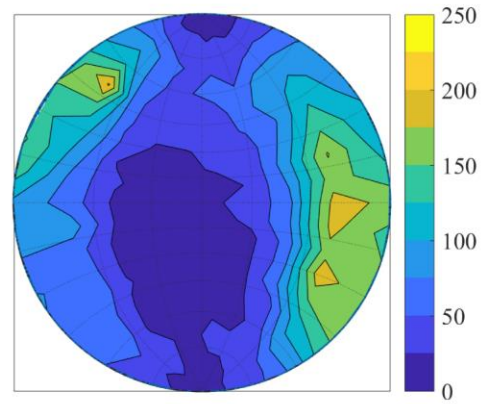
431

432 **Figure 7.** Distribution of pore unit orientations plotted on a lower hemisphere equal area stereographic projection

433 with a probability density contour.

434
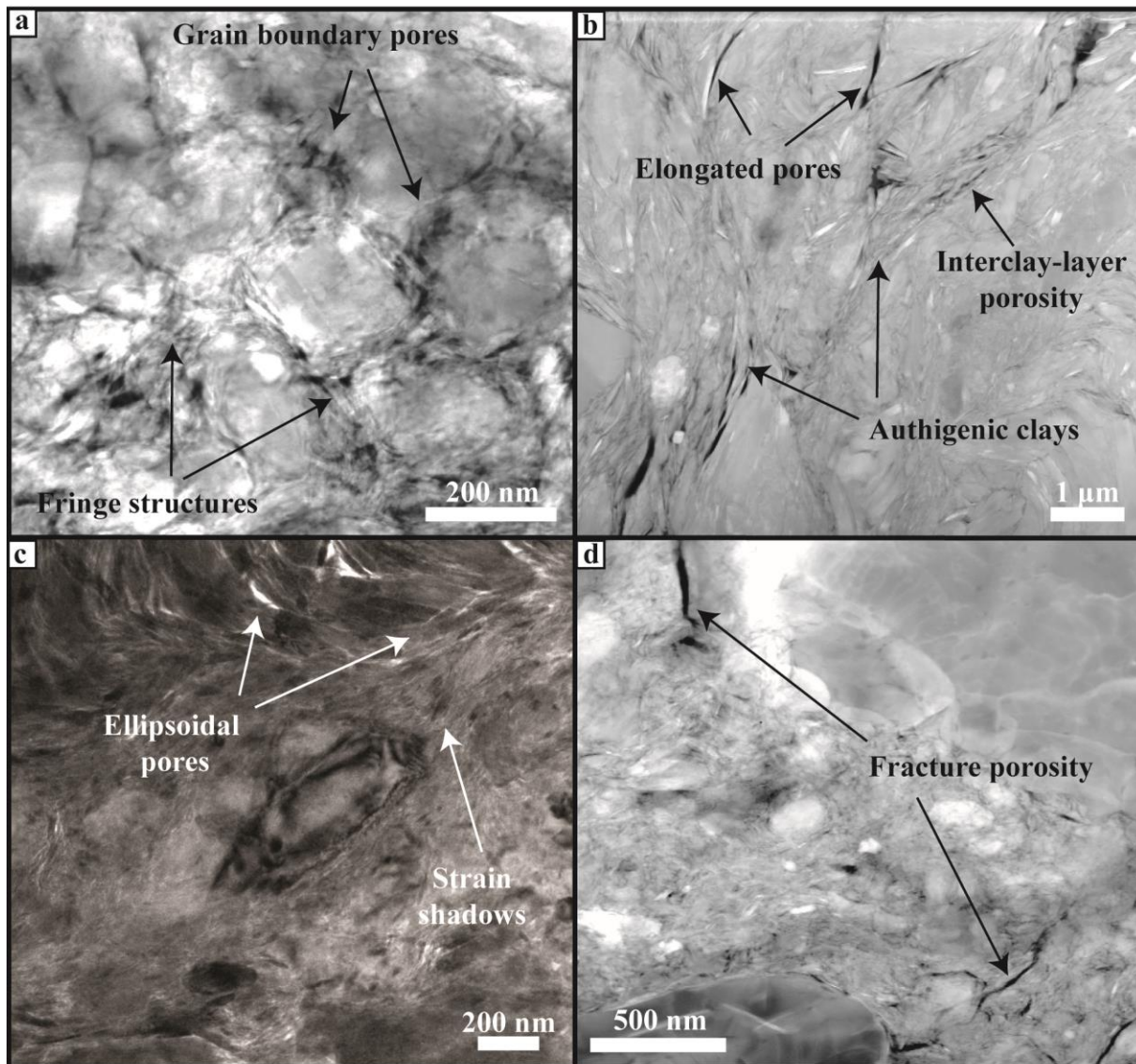
Figure 8. Transmission electron microscopy images collected from the gouge sample DFDP-1B 69_2.54 (PSZ-2).
(a) and (c) are bright-field images, where porosity appears as bright contrast areas. (b) and (d) are high-angle annular
dark field images, where pores appear as dark contrasts areas. (a) TEM bright-field image of homogeneous fault
gouge area. Quartz/feldspar grains, wrapped by fine authigenic clays, displaying fringe structures. Pores with sub-
angular shape distributed along grain boundaries. (b) HAADF image of phyllosilicate-rich gouge area. Co-existence
of fine authigenic clays with coarser clay mineral grains. Elongated pores and interlayer porosity. (c)TEM bright-
filed image of ellipsoidal pores in phyllosilicate-rich areas. Examples of strain shadows along quartz/feldspar grains.
(d) HAADF image of fracture porosity along grain boundaries of quartz/feldspar grains.